Environmental Science Nano

Emerging investigator series: First-principles and thermodynamics comparison of compositionally-tuned delafossites: Cation release from the (001) surface of complex metal oxides

Journal:	*Environmental Science: Nano*
Manuscript ID	EN-ART-11-2019-001304.R1
Article Type:	Paper

Complex metal oxide nanomaterials are broadly used as cathode materials in rechargeable batteries and industrially as heterogeneous catalysts. Chemical knowledge of how these materials transform and react in environmental settings is critical to understanding their interactions with biological systems. Here we used computational chemistry to posit and screen complex metal oxides with tailored aqueous cation release properties as a starting point for rational design of new electroactive materials with reduced negative environmental impact.

Emerging investigator series: First-principles and thermodynamics comparison of compositionally-tuned delafossites: Cation release from the (001) surface of complex metal oxides

Joseph W. Bennett,[a] Diamond T. Jones,[a] Blake G. Hudson,[a] Joshua Melendez-Rivera,[b] Robert J. Hamers,[c] and Sara E. Mason*[a]

Nanoscale complex metal oxides have transformed how technology is used around the world. A ubiquitous example is the class of electroreactive cathodes used in Li-ion batteries, found in portable electronics and electric cars. Lack of recycling infrastructure and financial drivers contribute to improper disposal, and ultimately, introduction of these materials into the environment. Outside of sealed operational conditions, it has been demonstrated that complex metal oxides can transform in the environment, and cause negative biological impact through leaching of cations into aqueous phases. Using a combined DFT and thermodynamics methodology, insights into the mechanism and driving forces of cation release can be studied at the molecular-level. Here, we describe design principles that can be drawn from previous collaborative research on com-plex metal oxide dissolution of the $Li(Ni_yMn_zCo_{1-y-z})O_2$ family of materials, and go on to posit ternary complex metal oxides in the delafossite structure type with controlled release behavior. Using equistoichiometric formulations, we use DFT and thermodynamics to model cation release. The trends are discussed in terms of lattice stability, solution chemistry/solubility limits, and elec-tronic/magnetic properties. Intercalation voltages are calculated and discussed as a predictive metric for potential functionality of the model materials.

1 Introduction

Manufacturing of nanoscale complex metal oxides (CMOs) is on the rise, concurrent with their use in mobile devices and renewable energy applications[1–3]. A key example is the delafossite structure type, which has found increased use as one of the prominent families of intercalation materials used in lithium-ion batteries (LIBs). The delafossite CMOs used in LIBs are the electroactive components of the cathode[4–7], and the prototypical example is $LiCoO_2$ (LCO). To decrease the cost and increase the performance of materials based on LCO, compositional tuning has led to $Li(Ni_yMn_zCo_{1-y-z})O_2$ (NMC) materials[8–11], in which the relative amount of each metal can be varied, such as high-Ni NMC compositions, which are readily synthesizable and demonstrate both high voltage in operation and enhanced cycle stability[12,13]. While compositionally tuned variants of LCO and NMC have been advantageous because of their improved properties and ease of manufacturing, they also contain transition metals whose release has been shown to be potentially toxic to a wide variety of organisms[14–21]. The proposed mechanisms of negative biological impact include both an increased concentration of potentially toxic cations in solution via incongruent CMO surface release of Ni and Co[14] and oxidative stress caused by the generation of reactive oxygen species (ROS) *in situ*[22].

To better understand the thermodynamics of surface transformations that enable cation release from the (001) structure, we evoke a DFT and thermodynamics approach, which we first applied to equistoichiometric NMC[7]. The modeling captures the experimentally observed trends in incongruent metal release from this surface (Li > Ni > Co > Mn)[14], and the electronic structure description of the NMC slabs provides insight about the interplay of tunable transition metal oxidation states and lattice stability. Importantly we were able to go on to inform experiments, such as recent work using Mn-rich and Ni-rich NMC compositions[23,24]. Briefly, the nominal valence of the cations in NMC are Ni^{2+}, Co^{3+}, and Mn^{4+} and the aqueous stable valences of these cations are Ni^{2+}, Co^{2+}, and Mn^{2+}. This means that releasing a Co or Mn from the (001) surface of NMC requires an additional reduction steps to the 2+ state, but the release of Ni^{2+} from NMC does not. Both experiment and our model agree that higher oxidation state metals, such as Mn^{4+}, are more resistant to surface release. This was supported by our recent work that studied NMC enriched

[a] Department of Chemistry, University of Iowa, Iowa City, IA 52242, USA.
[b] Department of Chemistry, The University of Puerto Rico at Cayey, Cayey PR 00737, USA.
[c] Department of Chemistry, University of Wisconsin-Madison, Madison, WI 53706, USA.
[8] email: sara-mason@uiowa.edu

with Mn; we found this created a population of Mn^{2+} in the solid state to maintain charge balance, and that this was more likely to be released than Mn^{4+}, even from the same surface[16,23]. Ni-rich formulations of NMC are of interest as well[25]. For these materials the opposite was true of Ni enriched NMC; more Ni^{3+} and Ni^{4+} were formed in the solid state to balance charge, and were less likely to be released from the surface than Ni^{2+} [24].Other computational studies have also reported on the increased presence of Ni^{3+} and Ni^{4+} in such Ni-rich formulations[26,27].

The DFT and thermodynamics mothodology provides chemical insight into how adjusting the composition within the NMC phase space tunes cation release from the surface in aqueous settings. Here, we aim to apply the model, along with known factors of metal toxicity and solubility, to posit and computationally screen ternary oxides (in the same delafossite structure) with tailored cation release behavior. In doing so, we identify metals that, at neutral or slightly acidic pH, are thermodynamically not favored to be released. Additionally, we also consider the use of metals that may be released, but are more innocuous to a wide range of organisms. If any of the model compositions are to be of practical use, then they must also be cost-effective replacements for elements such as Ni and Co, and demonstrate a comparable operating voltage, and as such factors of availability and computational cathode performance metrics are applied.

Here, we employ the DFT and thermodynamics methodology, and insights from our previous studies, to the task of rational design of ternary oxides. The hypothetical materials are proposed to have tailored cation release properties, and to preserve desirable properties for use as cathode materials. We here the survey of the rational design of ternary oxides for cathode materials with controlled cation release properties, we present here a survey of the properties of bulk and surface CMO compositions that include Ti, V, Mn, Fe, Co, Ni, Al. Each of these metals are less expensive than Co, can be found in octahedral coordination, and are known to form at least one stable cationic oxidation state between +2 and +4. We report on the bulk and surface structures, including the effects of delithiation and surface metal release to gauge the series of redox events that may take place while under standard operating conditions or exposed to aqueous environments. We create equistoichiometric compositions of general chemical formula $Li(A_{1/3}B_{1/3}C_{1/3})O_2$ such as $Li(Ni_{1/3}Mn_{1/3}Fe_{1/3})O_2$ (NMF) and $Li(Fe_{1/3}Ti_{1/3}V_{1/3})O_2$ (FTV) to compare to LCO and NMC. The sets of materials presented here are referred to as the generic 333-*ABC* delafossites, and Figure 1 shows how one could change composition from LCO to NMC to FMA to create comparable 333-*ABC* compositions. NMC is created from LCO by replacing 1/3 of the Co with Ni and 1/3 of the Co with Mn; FMA is created from NMC by replacing Ni with Fe and Co with Al.

The complete set of 333-*ABC* is as follows: $Li(Co_{1/3}Fe_{1/3}Al_{1/3})O_2$ (CFA), $Li(Ni_{1/3}Mn_{1/3}Co_{1/3})O_2$ (NMC), $Li(Ni_{1/3}Mn_{1/3}Al_{1/3})O_2$ (NMA), $Li(Ni_{1/3}Mn_{1/3}Fe_{1/3})O_2$ (NMF), $Li(Ni_{1/3}V_{1/3}Fe_{1/3})O_2$ (NVF), $Li(Fe_{1/3}Mn_{1/3}Al_{1/3})O_2$ (FMA), $Li(V_{1/3}Mn_{1/3}Al_{1/3})O_2$ (VMA), $Li(Fe_{1/3}Ti_{1/3}Al_{1/3})O_2$ (FTA), $Li(Fe_{1/3}Ti_{1/3}V_{1/3})O_2$ (FTV), and $Li(V_{1/3}Ti_{1/3}Al_{1/3})O_2$ (VTA). This set allows us to obtain insights into the thermodynamics of surface release of early transition metals such as Ti and V, and to compare with previous work on the surface dissolution of later transition metals such as Co and Ni[7,28,29]. Moreover, metals such as Ti, V, and Al are known to form stable oxides at pH values below 7[30,31], implying that surface release of these metals might be minimal at specific pH values, if they occur at all, and that they might impart additional lattice stabilization to prevent surface metal release. After analyzing trends in cation release, we present a set of design rules for the rational redesign of CMOs through compositional tuning, with an eye towards potentially reduced adverse interactions at the nano-bio interface and increased sustainability. We go on to suggest how the vacancy structures resulting from cation release could be used to create more sustainable catalytic systems for environmental/remediation applications.

2 Methods

All bulk and surface calculations employ spin-polarized periodic DFT calculations[32,33], and are carried out using Quantum Espresso, an open source software package[34]. Calculations are performed at the GGA level using the PBE-GGA[35] exchange-correlation functional. Justification of our choice of exchange-correlation functional is presented after the model details are presented. All atoms are represented as ultrasoft GBRV-type pseudopotentials[36,37]. Based on benchmarking reported in the initial GBRV design paper[37], and then expanded on by other studies[38], all calculations use a plane-wave cutoff of 40 Ry for the wavefunction and 320 Ry for the charge density. The convergence criterion for self-consistent relaxations was a maximum residual force of 5 meV/Å per atom, and all atoms are allowed to relax during structural optimizations. The bulk cells are based on a $[\sqrt{3}\times\sqrt{3}]R30^\circ$ rotated modification of the delafossite unit cell, to contain three octahedrally bound cations sites in a perfectly alternating manner. This modification also requires that the bulk cells be six layers, two lithium channels and six metal oxide layers, in the vertical direction, to maintain inversion symmetry critical to surface slab modeling[39], which is doubled compared to the delafossite unit cell. Owing to the relatively large cell size, all bulk calculations are found to be converged with respect to energy and force using a $6\times6\times3$ k-point grid[40].

The (001) delafossite surface is chosen for the present study based on matching experimentally characterized nanomaterial geometry (specifically, the (001) termination is reported to dominate synthesized naonsheets of NMC[14]) and as determined through *ab initio* thermodynamics investigations of LCO[41,42]. Previous experimental characterization showed that as-synthesized delafossite nanosheets have at least seven O-*M*-O layers[14], which would be computationally expensive for the supercell compositions that we are investigating. Therefore, the delafossite surface slabs used here include six total metal oxide layers (O-*M*-O), like the NMC surfaces in Refs.[7,23], of which the two interior and two exterior layers are related by inversion symmetry. The (001) surfaces presented here are based on a $[\sqrt{3}\times\sqrt{3}]R30^\circ$ rotated modification of the $LiCoO_2$ unit cell, where all $Li(A_{1/3}B_{1/3}C_{1/3})O_2$ surfaces have in plane dimensions of $2\sqrt{3}\times\sqrt{3}$ and at least 15 Å of vacuum separating each surface slab. This results in 6 total M per surface, where removal of 1 M

results in a 16.67% surface vacancy density. All $2\sqrt{3}\times\sqrt{3}$ surface relaxations, including defect structures for modeling metal release, use a $3\times6\times1$ k-point grid.

Some of the transition metals considered for inclusion in the ternary delafossites studied here can exist in multiple oxidation states. Furthermore, there are multiple magnetic ordering arrangements possible in the employed surface supercell. Spin coupling affects lattice stability, it is essential to include magnetic ordering in the DFT modeling. DFT energy minimization calculations do not sample all possible spin directions or ordering, and instead, for a given calculation, one must initialize the structure in terms of the magnetic moment (if any) on each atom, **m**, and the relative direction of the spin, **s**, on atoms in the lattice. Various spin orderings were tested and the results are shown in SI Table 1, where it is observed that AFM orderings are more favorable in the delafossite structure type. To initialize the the magnitude, **m**, and direction, **s**, on each transition metal, we take the number of d electrons in a given oxidation state, and assume a high-spin octahedral crystal field splitting, with the exception of d^6 which is taken to be low-spin. Upon geometry optimization and SCF minimization, the value/direction of **m**/**s** evolve, and details of initial and final values are given in Table 3. As presented later in detail, we employ a projected density of states analysis to assist in assigning formal oxidation states per metal, and those results are also presented in Table 3. Of note, in both NMF and NVF, there are two chemically distinct Fe atoms in the outermost metal layer of the surface, with Fe^{3+} being either low-spin (labeled NMF1 and NVF1 in Table 3) or high-spin (labeled NMF2 and NVF2 in Table 3). All of the inner-layer Fe show the low-spin behavior. The presence of high-spin Fe near the surface can be attributed to differences in the chemical environment in terms of connected oxygen functional groups. As shown in Figure 4 of the SI, some surface metal sites are connected to only bare oxygen, while others are connected to one or two OH groups. The high-spin Fe atoms in the NMF2 and NVF2 structures are connected only to bare oxygen atoms, while the low-spin surface Fe atoms are connected to one or two OH groups in NMF2 and NVF2, respectively. Similar results of surface functional groups relating to transition metal oxidation states was also reported in our previous work on Mn-rich NMC[23].

Aspects of the mechanism of cation release from the (001) delafossite surface have been studied previously at the DFT level[7], and are summarized here for clarity. We model the process of surface metal release (as the initial step of dissolution) step-wise. The first step is exchange of surface Li with H, and the second step is removing an H, O, and metal (M) from the (001) surface. We assume that the removal of any M-OH species results in a delocalization of electrons, since operation of Li-ion batteries relies upon the oxidation/reduction response of redox active M in the cathode. To compute the change in free energy associated with metal release, ΔG_{tot}, a DFT + solvent ion method[7,23,43,44] based on Hess's Law is employed. In the DFT + solvent ion method, ΔG_{tot} is partitioned between the computed energies of the reactants and products (used in ΔG_1) and experimental data (used in ΔG_2). DFT total energies are converted to Gibbs free energies (G) by the addition/subtraction of zero-point energy (ZPE) corrections and $T\Delta S$ terms, which are then used to calculate $\Delta G_1 = \Sigma G_{\text{products}} - \Sigma G_{\text{reactants}}$, where each G term is weighted appropriately by stoichiometric coefficients[7,43]. Also following previously reported details of the approach[42,43], corrective terms for surfaces are approximated per functional group. We assume that the minimum energy pathway of release involves removal of an M-OH unit as determined for NMC in previous work[7]. The total energies of M, O, and H released from the surface are for the atoms in their standard state, which implies that ΔG_1 can be used as a term that gauges relative lattice stability for the removal of an isolated M-OH unit per surface slab.

element	cation	pH	$\Delta G^{\circ}_{\text{SHE}}$ (eV)	solid	pH
Al	Al^{3+}(aq)	1-5	-5.027	Al_2O_3(s)	5-7
Ti	-	-	-	TiO_2(s)	1-7
V	VO^{2+}(aq)	1-5	-6.084	VO_2(s)	5-7
Mn	Mn^{2+}(aq)	1-7	-2.363	-	-
Fe	Fe^{2+}(aq)	1-6	-0.818	Fe_2O_3(s)	6-7
Co	Co^{2+}(aq)	1-7	-0.563	-	-
Ni	Ni^{2+}(aq)	1-7	-0.472	-	-

Table 1 For each element in the first column, the stable aqueous and solid species between pH values 1 to 7, and the pH range for which they will occur, are reported. The $\Delta G^{\circ}_{\text{SHE}}$ of each aqueous species is also tabulated, given in units of eV.

The second model term, ΔG_2, is based on the Nernst equation. $\Delta G_2 = \Delta G^{\circ}_{\text{SHE}}$ - $n_e e U_{\text{SHE}}$ - $2.303 n_{\text{H}^+} kT$ pH + kT ln a($H_xAO_y^{z-}$), where $\Delta G^{\circ}_{\text{SHE}}$ is the change in free energy of the aqueous cation/anion relative to the standard state, referenced to the standard hydrogen electrode (SHE). eU_{SHE} is the applied potential, relative to the SHE, and $H_xAO_y^{z-}$ are the concentrations of the released aqueous ions. Here we assume that no external potential is applied (U_{SHE}=0) and that ion concentrations are 1×10^{-6}M, an order of magnitude in line with measurements of released cations reported in experiment[14,16]. n_e and n_{H^+} are the number of electrons and protons involved in the chemical reactions required for surface release. They are zero for the aqueous species in the pH region of 1 to 7 investigated here, except for VO^{2+}, where n_e and n_{H^+} are 4 and 2, respectively, from the equation $V + H_2O \rightarrow VO^{2+} + 2H^+ + 4e^-$. Values of $\Delta G^{\circ}_{\text{SHE}}$ for each cation are obtained from Ref.[45] and are tabulated in units of eV in Table 1. Also found in Table 1 are the speciation of Al, Ti, V, Mn, Fe, Co, Ni for pH values 1-7 from DFT-computed Pourbaix diagrams.[46]

It is well-known that universal functionals such as PBE can fail to accurately predict the electronic structure of correlated materials, such as certain semiconductors and transition metal oxides, in what is often referred to as the "bandgap problem" in DFT[47–51]. In other works, some of the authors have investigated how the choice of functional affects the predictions of cation release using the DFT and thermodynamics method used in the present study. To summarize, in work by Bennett *et al.*[7], we first considered a DFT + U approach in modeling NMC. A complicating factor in using the $+U$ style of functionals in modeling these materials is that there is no guarantee that a U value that is optimal for a given transition metal in a binary oxide will provide the same level of

accuracy in the varied chemical environment of the complex oxide[52]. To this end, we tested five different sets of U values for the Ni, Co, and Mn atoms of the NMC structure. The resulting values of ΔG_1 showed non-monotonic behavior as a function of U, with each metal showing a different trend. For pure PBE and relatively small values of U (which are more chemically reasonable, larger values were explored for comparison), the experimentally observed trend in incongruent release is preserved. This supports that PBE results are capturing the relative trends in cation release, and this is in-line with other studies that report success in using PBE for modeling surface properties that are not bandgap dependent[53–55]. More recently, we compared the performance of different exchange-correlation functionals, including SCAN[56] and vdW-BEEF[57], in predicting cobalt release from LCO[58], and this benchmarking study also supports that PBE provides reasonable results overall. Further discussion of DFT approaches to modeling layered cathode materials can be found in a recent review article[59].

3 Results

3.1 Bulk structures

The bulk cell shown in Figure 2 is a $(\sqrt{3}\times\sqrt{3})$R30°$\times$ 2 modification of a hexagonal delafossite primitive cell as described in previous studies[42,60]. The bulk Li($A_{1/3}B_{1/3}C_{1/3}$)O_2 (333-*ABC*) cell contains four metal oxide layers (O-*M*-O). To create 333-*ABC* delafossite structure types, all equistoichiometric compositions contain metal cations bound in octahedra in a perfectly alternating manner that adheres to the trigonal symmetries of the underlying crystal structure. The metal ordering in each layer is shown on the left hand-side of Figure 2. The right hand-side shows a condensed version, 2 O-*M*-O and one lithium channel, of the vertical direction. Distances $d1$ and $d2$ describe the vertical O-*M*-O and O-Li-O distances, respectively, and are shown for each fully relaxed bulk 333-*ABC* in Table 2. The range of $d1$ is 2.07 (CFA) to 2.30 Å (FTV) and the range of $d2$ is 2.61 (NVF) to 2.67 Å (multiple); the vertical O-Li-O distance is less sensitive to metal substitution in our 11 compositions than the O-*M*-O distances. The differences in lattice constant a, $\approx$ 0.1 Å, is also less sensitive to compositional tuning than lattice constant c, where the change in c going from NMC to FTV is ≈0.5 Å. The third to last column in Table 2 is the band gap (E_{gap}) of the bulk materials. All 333-*ABC* materials studied here exhibit a bandgap, where the largest values of E_{gap} are for the compositions NMC (1.20 eV) and NMA (1.16 eV), and the smallest values of E_{gap} are found in the combinations NVF (0.18 eV) and FTV (0.17 eV). It is worth noting that owing to the use of the PBE functional, the calculated values of E_{gap} are systematically underestimated, though are expected to reflect trends[61]. We also report, in Table 2, theoretical enthalpies of formation, per formula unit (E_f), for all of the CMOs and found them to all be favorable and within a ≈28 eV range. Details of the enthalpy calculations can be found in section S1 in the SI.

Using the *ab initio* method of computing the intercalation voltage, V, we can assess the functionality of our proposed CMOs. The calculation of V requires the total energy of the CMOs with varying lithium content. For comparable systems, Ceder et al. measures the voltage for bulk NMC structures with 3 and 6 lithium atoms and finds that NMC should have a voltage of 3.0-4.5 V over the delithiation process[62]. In this work it is pointed out that finding the minimum energy structure for each level of delithiation step can be computationally taxing due the number of possible configurations. Specifically, for n Li atoms, a total of 2^n unique configurations can be formed in the bulk cell. To sidestep the issue of configurations, which would not provide chemical insights germane to the rational design of CMOs with controlled release profiles, we compare the fully lithiated structure, $Li_{1.00}$, and the fully delithiated structure, $Li_{0.00}$, to get a predicted voltage for each of our materials using Equation 1. This equation comes from the definition of the potential of a cell, which is defined as the decrease in Gibbs free energy per coulomb of charge transferred, or $E = \Delta G/-zF$[63,64]. In this equation, ΔG is energy of the products minus reactants where the fully lithiated structure is our starting point. With each Li removed from the cell, an electron will be lost. Thus -z can be expressed in terms of of the difference in lithium atoms between the fully lithiated material and the delithiathed form, denoted as $Li_{1.00}$-$Li_{0.00}$ in Equation 1. F is the Faraday constant. Our predicted voltages can be found in the last column of Table 2. To more completely map out the voltage profiles of the 333-*ABC* series would require smaller step sizes of successive Li removal.

As reported in Table 2, we observe that V increases with substitution of metals with Al, as shown by the difference in voltage for NMF (3.01 V) and NMA (3.60 V), and FTV (2.56 V) and FTA (3.02 V). This is a significant increase of at least 20%, which agrees with previous research[63,65]. We return to this trend, and offer chemical insight into its origin, after completing electronic structure analysis.

3.2 Effects of Compositional Tuning on Surface Properties

As noted in the Introduction, the oxidation states of metals in the lattice can be related to experimental dissolution trends for compositionally-tuned NMC. As described in the Methods section, we initialize values of **m** and directions of **s**, which evolve as a function of structural and electronic energy minimizations. The DFT computed values of $\mathbf{m}_{DFT}$ are not always intuitive, as some extent of spin relaxation occurs, and the chemical environment in the delafossite structure can result in complicated crystal field splitting. To recover a chemically intuitive description of the metals in each formulation, we carry out state-by-state, atom-by-atom projected density of states (PDOS) analysis for the surface structures of all CMO compositions. Using the PDOS plots in conjunction with the value of $\mathbf{m}_{DFT}$, we can arrive at formal values for the number of unpaired electrons ($\mathbf{m}_{formal}$) and integer oxidation states for each metal, as reported in Table 3. PDOS plots are presented in the Supplemental Information for surface cations in the CFA, NMC, NMA, NMF, and NVF compositions (SI Figure 2) and FMA, VMA, FTA, FTV, and VTA compositions (SI Figure 3).

In general, the oxidation states of the metals in the pristine surfaces (prior to the introduction of defects) are consistent across all formulations, with Co and Al always being 3^+, Ti being 4^+ and Ni always being 2^+, as shown in Table 3. Fe, Mn, and V are

the only metals with varied oxidation states from 2^+ to 4^+. The band gap (E_{gap}) was tabulated from the electronic band structure for the bulk and surface, with the surfaces having smaller values of E_{gap}, relative to bulk counterparts. The largest variation in E_{gap} was found in NMC, with a difference of 0.80 eV and the smallest was FTA and FTV with a 0.03 eV difference. We find that the values of E_{gap} for surfaces are not drastically different from those of the bulk solid solutions.

The PDOS analysis also provides insight into the aforementioned trends in V, specifically that substitution of a transition metal with Al in the C site always increases the intercalation voltage. As discussed by Aydinal *et al.*, delithiation is accompanied by donation of electron density to the oxygen $2p$ states in the lattice. As shown in Figure 3, when the C site is occupied by a transition metal, the oxygen $2p$ states are more delocalized, and show greater intensity just below the Fermi level. When Al is substituted, the PDOS of the oxygen $2p$ states show diminished intensity and less spread in energy near the Fermi level, which would impede the ability of these states to accept electron density and thereby driving up the value of V.

3.3 Thermodynamic Comparisons

We tabulate all values of ΔG_1, ΔG_2 (at pH 6), and ΔG_{tot} for the metals in the 333-*ABC* compositions in Table 4, to compare to the LCO parent structure where the ΔG_1 to release Co-OH from the (001) surface is 9.40 eV, and ΔG_2 (at pH 6) for Co is -9.68 eV. This yields an overall ΔG_{tot} = -0.28 eV for Co release from LCO at pH 6.

At pH 6, the preferred speciation of Al, Ti, V, and Fe are Al_2O_3(s), TiO_2(s), VO_2(s), and Fe_2O_3(s); ΔG_2 values for these species are undefined, so overall ΔG_{tot} is also undefined. Release of these species at pH 6 is not predicted to occur.

Figure 3 shows that substitution of Al with Fe, as in going from NMA to NMF, causes the Mn surface vacancy energy to decrease by $\approx$ 2 eV, such that Mn release from NMF is thermodynamically preferred relative to release from NMA or even NMC. Another example of significant change in ΔG_{tot} for Mn is seem in NMA and VMA: Substitution of Ni with V decreases ΔG_1 of Mn and Al by $\approx$ 4 and 3 eV, respectively. Focusing on Mn/Al compositions, replacing Fe with V going from FMA to VMA the ΔG_1 values of Mn are similar, and ΔG_1 values of Al change only by 0.4 eV. If Ni is present, as in NMA, ΔG_1 values of Mn and Al are both larger by $\approx$4 eV.

Comparing trends in values of ΔG_{tot} presented in Table 4, we find that compositional tuning has a significant effect on surface vacancy formation and subsequent metal release. Going from NMC to NMA to NMF to NVF the vacancy formation energy of Ni-OH successively decreases. Ni release is predicted to be favorable for all three 333-*ABC* combinations, and surface vacancy formation is most likely from NVF. When comparing the ΔG_1 of Ni for these four CMOs, where the higher values of ΔG_1 indicate higher lattice stability. Specifically, the combination of Mn/Al in NMA (8.27 eV) stabilizes Ni more-so than in NVF (6.07 eV). In this case, we explain the trends in surface energetics by the corresponding increased amount of unpaired spins on metal atoms in the surface.

In general, substituting Al for Co in NMC shows that Al-OH release is comparable to, or more energetically costly, than Co-OH removal. Substituting Ti for Mn (comparing FMA to FTA) shows that Ti-OH release is comparable to or more energetically costly than Mn-OH removal. Both Mn and Ti are consistently less prone to release than Co. It should also be noted that in the NMF and NVF compositions, it is thermodynamically more favorable to remove Fe than Co in NMC. This implies that Fe may be a beneficial substitution for Co in Mn and/or Ti-containing solid solutions.

Analysis of the surface energetics suggests that the absolute value of the total spin of the three transition metals per formula unit, denoted $|\Sigma \mathbf{m}_{formal}|$, can be used as a metric for predicting the lattice stability of the metal in the A-site. Following Table 5, in going from NMC to NMA, we observe a small change (0.09 eV) in the value of ΔG_1, where in the first material Co^{3+} (d^6, low-spin) is replaced with Al^{3+} (s^2p^6) which also has no spin. In the next case, going from NMA to NMF, the Al^{3+} is replaced with Fe^{3+} (d^5), high-spin. This causes the absolute total spin of the entire system to increase by 3.0. With this increase in spin, we also observe the ΔG_1 for Ni decrease by 0.92 eV. As we increase the absolute spin through compositional tuning, we expect the stability of the A transition metal within the lattice to decrease, allowing for easier removal/dissolution. We also observe this trend for compositions where the A metal is Fe and V. We find an exception when the A-site metal is Fe, shown in Table 6 with FTA, the only CMO with no spin on any of the metals, where it has a lower absolute total spin than FMA, but a higher ΔG_1. This is the only CMO formulation that was predicted to be non-magnetic, thus the spin-related trends do not track for the A-site metal. We also compared the average spins for each metal for the bulk, surface and vacancy structures shown in section S2 in the SI.

Across all compositions, Ni-OH release is the most thermodynamically favorable, and is highly dependent upon chemical environment. The DFT-computed ΔG_1 of Ni-OH release decreases in order as NMC > NMA > NMF > NVF. The fact that it is thermodynamically favorable to release Ni when Fe is present with Mn or V suggests that this might be a route towards easier metal reclamation in aqueous media. The release trend per ion (taken as ΔG_1, in eV, averaged over all compositions that contain that cation) is: Ti-OH (13.40) > Al-OH (12.47) > Mn-OH (11.30) > V-OH (10.34), Co-OH (10.33) > Fe-OH (8.35) > Ni-OH (7.51). On average, the d^0 elements Ti(IV) and Al(III) are the least likely to be released, the mid-d-block elements Mn, V, Co, and Fe are more prone to surface release, and the late 3d metal Ni is thermodynamically preferred for release.

4 Conclusions

We use a DFT and thermodynamics methodology to survey how compositional tuning of the delafossite structure affects metal release in an aqueous environment, in recent efforts to combine atomistic information obtained using DFT (in vacuum at 0 K) with macroscopic parameters that define operational and environmental conditions[66–68]. The model shows that cation release is tunable through changes in composition; it is thermodynamically

less favorable to create Ti or Al vacancies in the delafossite structure type than Fe or Ni. Elements such as V, Mn, and Fe were more likely to have a wide range of oxidation states than Ti, Ni, or Co, which were nominally Ti^{4+}, Ni^{2+}, and Co^{3+}. This implies that the mid 3*d*-block elements will assume oxidation states dictated by the presence of early and late 3*d*-block elements. The elements V and Ni were the first to change oxidation state with removal of a *M*-OH unit. These compositional changes alter the total spin of the material. When the total spin is increased, the dissolution of the metals becomes more favorable. We also tested to see if the functional properties of these materials were similar to industry standards such as NMC and LCO. We calculated the voltage, and found that the CMOs suggested are within the voltage range of NMC/LCO. Replacing metals with Al will increase the voltage, suggesting a more functional battery.

The set of 333-*ABC* compositions presented here yields insights into further developing technologies based on the CMO surface and its interface with aqueous media or the gas phase. For example, there has been a large effort to replace the toxic and flammable organic electrolytes in LIBs to those that are aqueous since 1994[69]. LIBs with aqueous electrolytes, aqueous lithium-ion batteries (ALIBs), have the potential to be safer with cheaper production costs, and up to two orders of magnitude higher ionic conductivity than their non-aqueous counterparts[70]. Unfortunately, many of these initial batteries have low cycleability due to instability of the compounds used for the electrodes[71]. More specifically, when lithium intercalation compounds such as $LiMn_2O_4$, LCO, and NMC, were used as the cathode, it was found that the pH of the electrolyte was important for the stability of the cathode[72]. Therefore, the stability of these materials in aqueous environments, i.e. solubility[73] must be considered for use in the new frontier of high energy storage.

We also note that understanding the pH dependent behavior of CMO compositions is key to devising new strategies for cost-effective aqueous material processing[74], increasing battery longevity[75], and how CMOs might break down in the environment[76]. Recent work has pointed towards the use of waste CMOs as catalysts for the surface adsorption and oxidation of organic compounds[77]. The acid-assisted leaching of Li and Co cations to create surface vacancies in LCO was shown to adsorb and oxidize benzene, but the pH-dependent thermodynamics of surface metal release and structures presented here could be used as a guide for design of more specific, tailorable catalytic systems.

As computational materials science continues to develop as a means for materials discovery and optimization, it can also serve as a valuable tool for understanding the molecular-level details of nanomaterial transformations in the environment, and developing rational strategies to reduce negative biological impacts. First-principles calculations provide perfect atomistic control, which can be used to systematically study how composition and geometry influence electronic structure and solid-state properties. Using DFT information in conjunction with thermodynamics modeling enables connection to real-world conditions, and circumvents current challenges in modeling aqueous effects directly. Looking forward, developing robust means for modeling the interfacial chemistry of CMOs will be essential for further understanding their transformations and reactivity in the environment.

Conflicts of interest

There are no conflicts to declare.

Acknowledgements

This work was supported by National Science Foundation under the Center for Sustainable Nanotechnology, CHE-1503408. The CSN is part of the Centers for Chemical Innovation Program. This research was supported in part through computational resources provided by The University of Iowa, Iowa City, Iowa and the National Science Foundation grant CHE-0840494. This work used the Extreme Science and Engineering Discovery Environment (XSEDE[78]), which is supported by National Science Foundation grant number ACI-1548562 through allocation ID TG-GEO160006. J.W.B. and S.E.M. thank Profs. Christy Haynes and Rebecca Klaper for useful discussions of this work.

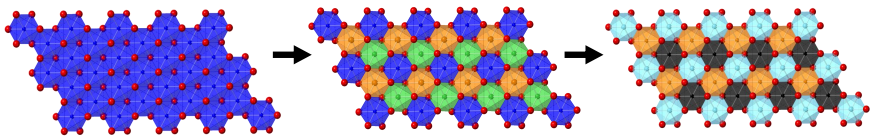

Fig. 1 From left to right are top-down depictions of $LiCoO_2$ (LCO), $Li(Ni_{1/3}Mn_{1/3}Co_{1/3})O_2$ (NMC), and $Li(Fe_{1/3}Mn_{1/3}Al_{1/3})O_2$ (FMA) layers, which are formed using successive equistoichiometric metal substitutions of the delafossite structure type. Metal identity is indicated by color as: Ni (green), Mn (orange), Co (dark blue), Al (black), and Fe (light blue). All red spheres are O.

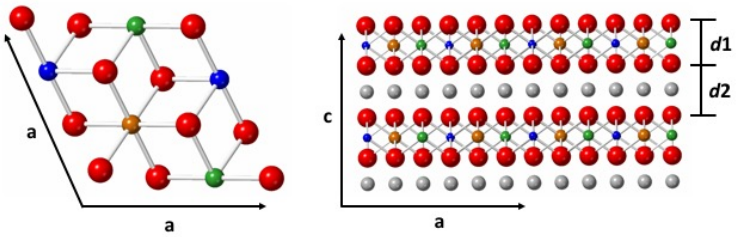

Fig. 2 (Left) Top view of a metal oxide layer of the $\sqrt{3} \times \sqrt{3}$ R30° bulk 333-ABC cell. (Right) Side view of the layer ordering in bulk 333-ABC, with layer spacings $d1$ (O-M-O) and $d2$ (O-Li-O). Metal identity is indicated by color as: Ni (green), Mn (orange), Co (dark blue), Al (black), and Fe (light blue). Li is depicted as gray and O is red.

	a (Å)	c (Å)	$d1$ (Å)	$d2$ (Å)	E_{gap} (eV)	E_f (eV)	Voltage (V)
LCO	2.848	14.032	2.03	2.64	1.12	-55.56	3.56
CFA	2.840	14.233	2.07	2.67	0.74	-38.93	3.38
NMC	2.883	14.232	2.12	2.62	1.20	-53.48	3.17
NMA	2.879	14.327	2.12	2.65	1.16	-39.21	3.60
NMF	2.922	14.442	2.20	2.62	0.58	-51.13	3.01
NVF	2.918	14.552	2.24	2.61	0.18	-47.89	2.89
FMA	2.836	14.378	2.13	2.67	0.35	-34.66	3.05
VMA	2.856	14.552	2.18	2.67	0.28	-29.51	2.68
FTA	2.931	14.582	2.19	2.67	1.04	-40.33	3.02
FTV	2.934	14.771	2.30	2.62	0.17	-36.95	2.56
VTA	2.910	14.614	2.20	2.67	0.44	-25.03	2.47

Table 2 DFT minimum energy lattice parameters a and c, Å of the bulk ternary delafossite materials. Also reported are interlayer spacings $d1$ and $d2$, in units of Å. DFT-computed values of the electronic bandgap, E_{gap} and formation enthalpy per formula unit, E_{f}, are reported, both in eV. The calculated averaged voltage is reported in units of V.

$$V = \frac{E[Li_{0.00}(A_{1/3}B_{1/3}C_{1/3})O_2] + E(Li_{metal}) * (Li_{1.00} - Li_{0.00}) - E[Li_{1.00}(A_{1/3}B_{1/3}C_{1/3})O_2]}{(Li_{1.00} - Li_{0.00}) * F} \quad (1)$$

	$\mathbf{s}_{\text{Initial}}$	$\mathbf{s}_{\text{Final}}$, $\mathbf{m}_{\text{DFT}}$ (μ_B), ($\mathbf{m}_{\text{formal}}$ (μ_B))			Metal & formal oxidation state	E_{gap} (eV)
	A, *B*, *C*	*A*	*B*	*C*	*A*, *B*, *C*	
CFA	↓, ↑, ↓	-, 0.00, (0)	↑, 0.86, (1)	-, 0.00, (0)	Co^{3+}, Fe^{3+} , Al^{3+}	0.02
NMC	↓, ↑, ↓	↓, 1.45, (2)	↑, 2.46, (3)	↓, 0.01, (0)	Ni^{2+}, Mn^{4+}, Co^{3+}	0.40
NMA	↑, ↓, ↓	↑, 1.43, (2)	↓, 2.30, (3)	↓, 0.01, (0)	Ni^{2+}, Mn^{4+} , Al^{3+}	0.85
NMF1	↑, ↑, ↓	↑, 1.42, (2)	↑, 2.44, (3)	↓, 0.86, (1)	Ni^{2+}, Mn^{4+}, Fe^{3+}	0.05
NMF2				↓, 3.47, (5)	Ni^{2+}, Mn^{4+}, Fe^{3+}	0.05
NVF1	↑, ↑, ↓	↑, 1.42, (2)	↓, 0.31, (1)	↑↓, 0.10,(1)	Ni^{2+}, V^{4+} , Fe^{3+}	-
NVF2				↓, 3.55, (5)	Ni^{2+}, V^{4+} , Fe^{3+}	-
FMA	↓, ↑↓, ↓	↓, 0.17, (0)	↑↓,2.23, (3)	-,0.00 (0)	Fe^{2+}, Mn^{4+}, Al^{3+}	0.17
VMA	↑, ↓, ↓	↑,1.39, (2)	↓, 1.64, (2)	-, 0.00, (0)	V^{3+}, Mn^{3+}, Al^{3+}	0.21
FTA	↑, ↓, ↓	-, 0.00, (0)	-, 0.00, (0)	-, 0.00, (0)	Fe^{2+}, Ti^{4+}, Al^{3+}	1.07
FTV	↑, ↓, ↓	-, 0.01, (0)	- , 0.11, (0)	↓, 1.29, (2)	Fe^{2+}, Ti^{4+} , V^{3+}	0.14
VTA	↑, ↓, ↓	↑, 1.70, (3)	↑, 0.29, (0)	-,0.00, (0)	V^{2+}, Ti^{4+} , Al^{3+}	0.37

Table 3 Details of initialized spin direction per metal atom ($\mathbf{s}_{\text{Initial}}$), final spin direction per atom ($\mathbf{s}_{\text{Final}}$), DFT calculated magnetic moment per atom ($\mathbf{m}_{\text{DFT}}$, μ_B), assigned formal magentic moment per atom ($\mathbf{m}_{\text{formal}}$, μ_B), metal identify/formal assigned oxiation state, and calculated eletronic bandgap values (E_{gap}, eV), for the ten modeled ternary delafossites. *A*, *B*, and *C* refer to the three unique metal sites per formula unit. Spin directions are reported using an up arrow (↑) or down arrow (↓). Double opposing arrows (↑↓) are used to denote when the spin on a given metal is antiferromagnetically coupled with the same metal site in the neighboring formula unit in the supercell. For metals which relax to having a neglibile magnetic moment, a "-" is used instead of the arrow notation. For NMF and NVF, there are two distinct surface Fe sites that are either low-spin (in NMF1 and NVF1) or low-spin Fe^3 (in NMF2 and NVF2), discussed in more detail in the text. All inner-layer Fe in both NMF and NVF exhibit low-spin Fe^{3+} electronic structure.

	A	ΔG_1	ΔG_2	ΔG_{tot}	*B*	ΔG_1	ΔG_2	ΔG_{tot}	*C*	ΔG_1	ΔG_2	ΔG_{tot}
LCO	Co	9.40	-9.68	-0.28	-	-	-	-	-	-	-	-
CFA	Co	9.76	-9.68	+0.08	Fe	8.91	-	-	Al	13.28	-	-
NMC	Ni	8.36	-9.59	-1.23	Mn	12.46	-11.48	+0.98	Co	9.72	-9.68	+0.04
NMA	Ni	8.27	-9.59	-1.32	Mn	13.45	-11.48	+1.97	Al	14.42	-	-
NMF	Ni	7.35	-9.59	-2.24	Mn	11.25	-11.48	-0.23	Fe	9.78	-	-
NVF	Ni	6.07	-9.59	-3.52	V	12.00	-	-	Fe	8.15	-	-
FMA	Fe	7.31	-	-	Mn	9.68	-11.48	-1.80	Al	11.54	-	-
VMA	V	9.89	-	-	Mn	9.67	-11.48	-1.81	Al	11.10	-	-
FTA	Fe	7.72	-	-	Ti	14.39	-	-	Al	12.82	-	-
FTV	Fe	8.23	-	-	Ti	13.25	-	-	V	10.22	-	-
VTA	V	9.27	-	-	Ti	12.55	-	-	Al	11.68	-	-

Table 4 Thermodynamics of release at pH 6 for each cation of the 333-*ABC* compositions. The DFT-computed ΔG_1 values are added to ΔG_2 values to obtain ΔG_{tot} values for each cation *A*, *B*, and *C*. All values are reported in units of eV, and a - indicates than the thermodynamically preferred species is a solid phase.

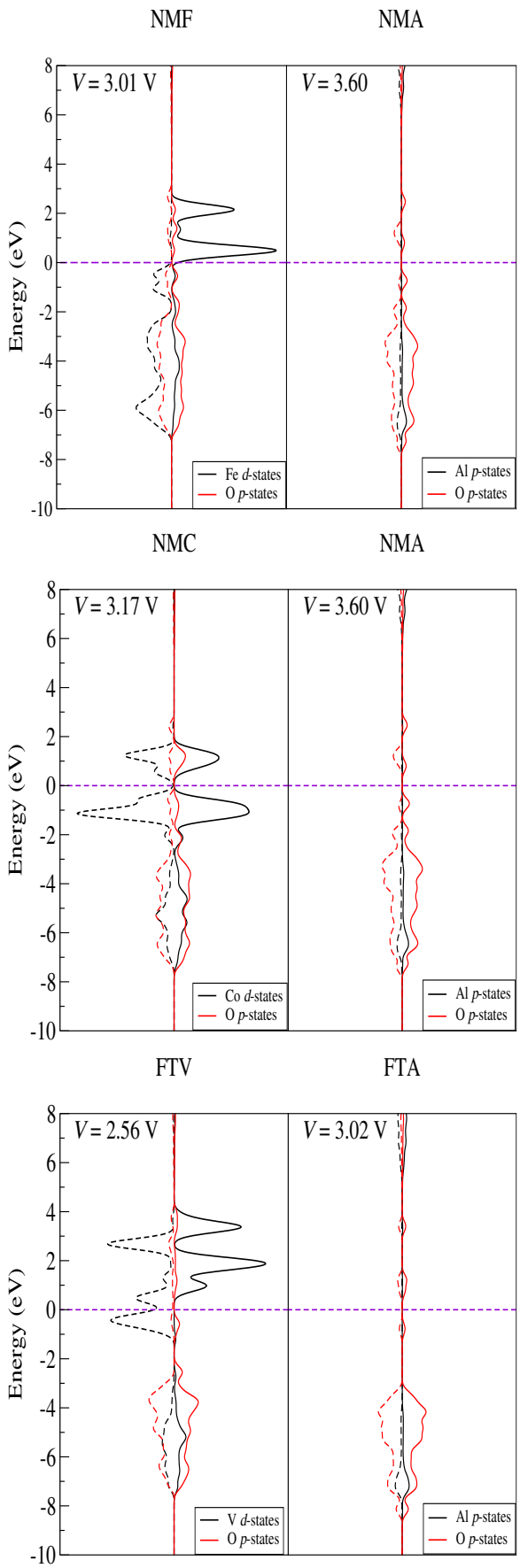

Fig. 3 PDOS comparing the effects of substituting with Al in fully lithiated bulk structures. On the left of each plot is the valence electron density of the transition metal (black) to be substituted with Al and the O states (red). Dashed lines represent spin down density, and solid lines are spin up. The fermi energy is set to zero and shown as a purple dashed line. (a) NMF and NMA (b) NMC and NMA (c) FTV and FTA.

CMO	$\Delta G_1(A)$	$\mathbf{s}_{\text{Final}}$, $\mathbf{m}_{\text{formal}}$ (μ_B)			$\lvert\Sigma\mathbf{m}_{\text{formal}}\rvert$, μ_B
		A	B	C	
VMA	9.98	↑, 3.0	↓, 3.0	-, 0.0	0.0
VTA	9.36	↑, 3.0	-, 0.0	-, 0.0	3.0
NMC	8.45	↑, 2.0	↓, 3.0	-, 0.0	1.0
NMA	8.36	↑, 2.0	↓, 3.0	-, 0.0	1.0
NMF	7.44	↑, 2.0	↓, 3.0	↑, 5.0	4.0
NVF	6.16	↑, 2.0	↓, 1.0	↑, 5.0	6.0

Table 5 Values of ΔG_1 at pH 6 when the A-site metal is V (top two rows) or Ni (bottom four rows) and the composition is varied stepwise. Also reported are the spin directions on each metal site (A, B, and C) in the DFT optimied geometry ($\mathbf{s}_{\text{Final}}$, denoted using ↑, ↓, or "-" when there is no net spin), and the formal magnetic moments (μ_{formal}, μ_B). The final column sums the absolute value of the formal magnetic moments, deonted as $\lvert\Sigma\mathbf{m}_{\text{formal}}\rvert$, in units of μ_B.

CMO	$\Delta G_1(A)$	$\mathbf{s}_{\text{Final}}$, $\mathbf{m}_{\text{formal}}$ (μ_B)			$\lvert\Sigma\mathbf{m}_{\text{formal}}\rvert$, μ_B
		A	B	C	
FTV	8.32	-, 0.0	-, 0.0	↑, 2.0	2.0
FTA	7.81	-, 0.0	-, 0.0	-, 0.0	0.0
FMA	7.40	-, 0.0	↓, 3.0	-, 0.0	3.0

Table 6 Values of ΔG_1 at pH 6 of where the A-site metal is Fe. Also reported are the spin directions on each metal site (A, B, and C) in the DFT optimied geometry ($\mathbf{s}_{\text{Final}}$, denoted using ↑, ↓, or "-" when there is no net spin), and the formal magnetic moments (μ_{formal}, μ_B). The final column sums the absolute value of the formal magnetic moments, deonted as $\lvert\Sigma\mathbf{m}_{\text{formal}}\rvert$, in units of μ_B.

References

1 T. P. Narins, *Extractive Industries and Society*, 2017, **4**, 321–328.

2 E. A. Olivetti, G. Ceder, G. G. Gaustad and X. Fu, *Joule*, 2017, **1**, 229–243.

3 R. J. Hamers, *Acc. Chem. Res.*, 2017, **50**, 633–637.

4 J. Lu, Z. Chen, Z. Ma, F. Pan, L. A. Curtiss and K. Amine, *Nature Nanotech.*, 2016, **11**, 1031–1038.

5 L. A.-W. Ellingsen, C. R. Hung, G. Majeau-Bettez, B. Singh, Z. Chen, M. S. Whittingham and A. H. Stromman, *Nature Nanotech.*, 2016, **11**, 1039–1051.

6 D. Larcher and J.-M. Tarascon, *Nature Chem.*, 2014, **7**, 19–29.

7 J. W. Bennett, D. Jones, X. Huang, R. J. Hamers and S. E. Mason, *Environ. Sci. Technol.*, 2018, **52**, 5792–5802.

8 B. J. Hwang, Y. W. Tsai, D. Carlier and G. Ceder, *Chem. Mater.*, 2003, **15**, 3676–3682.

9 Y.-K. Sun, Z. Chen, H.-J. Noh, D.-J. Lee, H.-G. Jung, Y. Ren, S. Wang, C. S. Yoon, S.-T. Myung and K. Amine, *Nature Mater.*, 2012, **11**, 942–947.

10 N. S. Choi, Z. Chen, S. A. Freunberger, X. Ji, Y. K. Sun, K. Amine, G. Yushin, L. F. Nazar, J. Cho and P. G. Bruce, *Angew. Chem. Int. Ed.*, 2012, **51**, 9994–10024.

11 P. Rozier and J.-M. Tarascon, *J. Electrochem. Soc.*, 2015, **162**, A2490–A2499.

12 W. Zhao, J. Zheng, L. Zou, H. Jia, B. Liu, H. Wang, M. H. Engelhard, C. Wang, W. Xu, Y. Yang and J.-G. Zhang, *Adv. Energy Mater.*, 2018, **8**, 1800297.

13 P. Yan, J. Zheng, J. Liu, B. Wang, X. Cheng, Y. Zhang, X. Sun, C. Wang and J.-G. Zhang, *Nature Energy*, 2018, **3**, 600–605.

14 M. N. Hang, I. L. Gunsolus, H. Wayland, E. S. Melby, A. C. Mensch, K. R. Hurley, J. A. Pedersen, C. L. Haynes and R. J. Hamers, *Chem. Mater.*, 2016, 1092–1100.

15 M. Dogangun, M. N. Hang, J. Machesky, A. C. McGeachy, N. Dalchand, R. J. Hamers and F. M. Geiger, *J. Phys. Chem. C.*, 2017, **121**, 27473–27482.

16 I. L. Gunsolus, M. N. Hang, N. V. Hudson-Smith, J. T. Buchman, J. W. Bennett, D. Conroy, S. E. Mason, R. J. Hamers and C. L. Haynes, *Environ. Sci.: Nano.*, 2017, **4**, 636–646.

17 J. Bozich, M. Hang, R. J. Hamers and R. Klaper, *Environ. Toxicology and Chem.*, 2017, **36**, 2493–2502.

18 M. N. Hang, N. V. Hudson-Smith, P. L. Clement, Y. Zhang, C. Wang, C. L. Haynes and R. J. Hamers, *ACS Appl. Nano Mater.*, 2018, **4**, 1721–1730.

19 Z. V. Feng, B. R. Miller, T. G. Linn, T. Pho, K.-N. L. Hoang, M. N. Hang, S. L. Mitchell, R. T. Hernandez, E. E. Carlson and R. J. Hamers, *Environ. Sci.: Nano.*, 2019, **6**, 305–314.

20 Y. Cui, E. S. Melby, A. C. Mensch, E. D. Laudadio, M. N. Hang, A. Dohnalkova, D. Hu, R. J. Hamers and G. Orr, *Nano Lett.*, 2019, **19**, 1990–1997.

21 N. J. Niemuth, B. J. Curtis, M. N. Hang, M. J. Gallagher, D. H. Fairbrother, R. J. Hamers and R. D. Klaper, *Environ. Sci. Technol.*, 2019, **53**, 3860–3870.

22 T. A. Qiu, M. J. Gallagher, N. V. Hudson-Smith, J. Wu, M. O. P. Krause, J. D. Fortner and C. L. Haynes, *Environ. Sci.: Nano*, 2016, **3**, 940–945.

23 J. W. Bennett, D. T. Jones, R. J. Hamers and S. E. Mason, *Inorg. Chem.*, 2018, **57**, 13300–13311.

24 J. T. Buchman, E. A. Bennett, C. Wang, A. Abbaspour Tamijani, B. G. Hudson, C. M. Green, P. L. Clement, B. Zhi, A. H. Henke, E. D. Laudadio, S. E. Mason, R. J. Hamers, R. D. Klaper and C. L. Haynes, *Environ. Sci.: Nano.*, 2020, **7**, 571–587.

25 F. Schipper, E. M. Erikson, C. Erk, J.-Y. Shin, F. F. Chesneau and D. Aurbach, *J ELECTROCHEM SOC*, 2017, **164**, 6220–6228.

26 M. Dixit, B. Markovsky, F. Schipper, D. Aurbach and D. T. Major, *J. Phys. Chem.*, 2017, **121**, 22628–22636.

27 M. Dixit, M. Kosa, O. S. Lavi, B. Markovsky, D. Aurbach and D. T. Major, *Phys. Chem. Chem. Phys.*, 2016, **18**, 6799–6812.

28 J. T. Buchman, C. W. Evan A. Bennett, A. AbbaspourTamijani, J. W. Bennett, B. G. Hudson, C. M. Green, P. L. Clement, B. Zhi, A. Henke, E. D. Laudadio, S. E. Mason, R. J. Hamers, R. D. Klaper and C. L. Haynes, *Environ. Sci.: Nano*, 2019, DOI: 10.1039/c9en01074b.

29 A. AbbaspourTamijani, J. W. Bennett, D. T. Jones, N. Cartagena-Gonzalez, Z. R. Jones, E. D. Laudadio, R. J. Hamers, J. A. Santana and S. E. Mason, 2019, DOI: 10.26434/chemrxiv.9764774.v1.

30 W. G. Cook and R. P. Olive, *Corros. Sci.*, 2012, **58**, 291–298.

31 X. Zhou, C. Wei, M. Li, S. Qiu and X. Li, *Hydrometallurgy*, 2011, **106**, 104–112.

32 P. Hohenberg and W. Kohn, *Phys. Rev.*, 1964, **136**, B864–71.

33 W. Kohn and L. J. Sham, *Phys. Rev.*, 1965, **140**, A1133–8.

34 P. Giannozzi, S. Baroni, N. Bonini, M. Calandra, R. Car, C. Cavazzoni, D. Ceresoli, G. L. Chiarotti, M. Cococcioni, I. Dabo and et al., *J. Phys.:Condens. Matter*, 2009, **21**, 395502–20.

35 J. P. Perdew, K. Burke and M. Ernzerhof, *Phys. Rev. Lett.*, 1996, **77**, 3865–8.

36 D. Vanderbilt, *Phys. Rev. B Rapid Comm.*, 1990, **41**, 7892–5.

37 K. F. Garrity, J. W. Bennett, K. M. Rabe and D. Vanderbilt, *Comp. Mater. Sci.*, 2014, **81**, 446–452.

38 G. Pranini, A. Marrazzo, I. E. Castelli, N. Mounet and N. Marzari, *Npj Comput. Mater.*, 2018, **4**, 1–12.

39 K. W. Corum, X. Huang, J. W. Bennett and S. E. Mason, *Molecular Simulation*, 2017, **43**, 406–419.

40 H. J. Monkhorst and J. D. Pack, *Phys. Rev. B*, 1976, **13**, 5188–5192.

41 D. Kramer and G. Ceder, *Chem. Mater.*, 2009, **21**, 3799–3809.

42 X. Huang, J. W. Bennett, M. N. Hang, E. D. Laudadio, R. J. Hamers and S. E. Mason, *J. Phys. Chem. C.*, 2017, **121**, 5069–5080.

43 X. Rong and A. M. Kolpak, *J. Phys. Chem. Lett.*, 2015, **6**, 1785–1789.

44 X. Rong, J. Parolin and A. M. Kolpak, *ACS Catal.*, 2016, **6**, 1153–1158.

45 D. D. E. Wagman, I. Halow, V. B. Parker, S. M. Bailey and R. H. Schumm, *National Bureau of Standards*, 1971, 1 – 272.

46 K. A. Persson, B. Waldwick, P. Lazic and G. Ceder, *Phys. Rev. B.*, 2012, **85**, 235438.

47 M. K. Y. Chan and G. Ceder, *PRL*, 2010, **105**, 196403–196403.

48 K. A. Johnson and N. W. Ashcroft, *Phys. Rev. B*, 1998, **58**, 15548.

49 J. P. Perdew, *Int. J. Quantum Chem.*, 1985, **28**, 497–523.

50 A. Seidl, A. Gorling, P. Vogl, J. A. Majewski and M. Levy, *Phys. Rev. B.*, 1996, **53**, 3764.

51 A. J. Cohen, P. Mori-Sanchez and W. Yang, *Science*, 2008, **321**, 792–794.

52 J. W. Bennett, B. G. Hudson, I. K. Metz, S. Spurgeon, Q. Cui and S. E. Mason, *Comp. Mat. Sci.*, 2019, **170**, 109137.

53 A. Tilocca and A. Selloni, *J. Phys. Chem. C*, 2002, **116**, 9114–21.

54 K. Leung, *J. Phys. Chem. C*, 2012, **116**, 9852–9861.

55 N. N. Intan, K. Klyukin and V. Alexandrov, *ACS Appl. Mater.*, 2019, **11**, 20110–20116.

56 J. Sun, A. Ruzsinsky and J. P. Perdew, *Phys. Rev. Lett.*, 2015, **115**, 1–6.

57 J. Wellendroff, K. T. Lundgaard, A. Mogelhoj, V. Petzold, D. D. Landis, J. K. Norskon, T. Bligaard and K. W. Jacobsen, *Phys. Rev. B*, 2012, **85**, 1–23.

58 A. A. Tamijani, J. W. Bennett, D. T. Jones, N. Cartagena-Gonzalez, Z. R. Jones, E. D. Laudadio, R. J. Hamers, J. A. Santana and S. E. Mason, *Appl. Surf. Sci.*, 2020, **515**, 145865.

59 A. Chakraborty, S. Kunnikuruvan, S. Kumar, B. Markovsky, D. Aurbach, M. Dixit and D. T. Major, *Chem. Mater.*, 2020, **32**, 915–952.

60 Y. Koyama, N. Yabuuchi, I. Tanaka, H. Adachi and T. Ohzuku, *J. ELectrochem. Soc.*, 2004, **151**, A1545–A1551.

61 J. W. Bennett, I. Grinberg and A. M. Rappe, *JACS*, 2008, **130**, 17409 – 17412.

62 B. J. Hwang, Y. W. Tsai, D. Carlier and G. Ceder, *Chem. Mater.*, 2003, **15**, 3676–3682.

63 G. Ceder, Y.-M. Chiang, D. R. Sadoway, M. K. Aydinol, Y.-I. Jang and B. Huang, *Nature*, 1998, **392**, 694–696.

64 J. B. Goodenough and K.-S. Park, *J. Am. Chem. Soc.*, 2013, **135**, 1167–1176.

65 M. K. Aydinol, A. F. Kohn, G. Cedar, K. Cho and J. Joannopoulos, *Phys. Rev. B*, 1997, **56**, 1354–1365.

66 L. Grajciar, C. J. Heard, A. A. Bondarenko, M. V. Polynski, J. Meeprasert, E. A. Pidko and P. Nachtigall, *Chem. Soc. Rev.*, 2018, **47**, 8307–8348.

67 J. P. Janet, F. Liu, A. Nandy, C. Duan, T. Yang, S. Lin and H. J. Kulik, *Inorg. Chem.*, 2019, **58**, 10592 – 10606.

68 J. E. D. Vrieze, G. T. K. K. Gunasooriya, J. W. THybaut and M. Saeys, *Current Opinion in Chem. Eng.*, 2019, **23**, 85–91.

69 W. Li, J. R. Dahn and D. S. Wainwright, *Science*, 1994, **264**, 1115–1118.

70 M. Armand and J. M. Tarascon, *Nature*, 2008, **451**, 652–657.

71 D. Bin, Y. Wen, Y. Wang and Y. Xia, *Journal of Energy Chem.*, 2018, **27**, 1521–1535.

72 Y. gang Wang, J. yan Luo, C. xiao Wang and Y. yao Xia, *Elec. Soc. S.*, 2005, **153**, 1425–1431.

73 J.-Y. Luo, W.-J. Cui and P. H. an Yong-Yao Xia, *Nat. Chem.*, 2010, **2**, 760–765.

74 M. Bichon, D. Sotta, N. Dupre, E. D. Vito, A. Boulineau, W. Porcher and B. Lestriez, *ACS Appl. Mater. Interfaces*, 2019, **11**, 18331–18341.

75 W. D. Richards, L. J. Miara, Y. Wang, J. C. Kim and G. Ceder, *Chem. Mater.*, 2016, **28**, 266–273.

76 E. Billy, M. Joulie, R. Laucournet, A. Boulineau, E. DeVito and D. Meyer, *ACS Appl. Mater. Interfaces*, 2018, **10**, 16424–16435.

77 T. Dai, H. Zhou, Y. Liu, R. Cao, J. Zhan, L. Liu and B. W.-L. Jang, *ACS Sustainable Chem. Eng.*, 2019, **7**, 5072–5081.

78 J. Towns, T. Cockerill, M. Dahan, I. Foster, K. Gaither, A. Grimshaw, V. Hazlewood, S. Lanthrop, D. Lifka, G. D. Peterson, R. Roskies, J. R. Scott and N. Wilkins-Diehr, *Comp. Sci. Engineering*, 2014, **16**, 62–74.

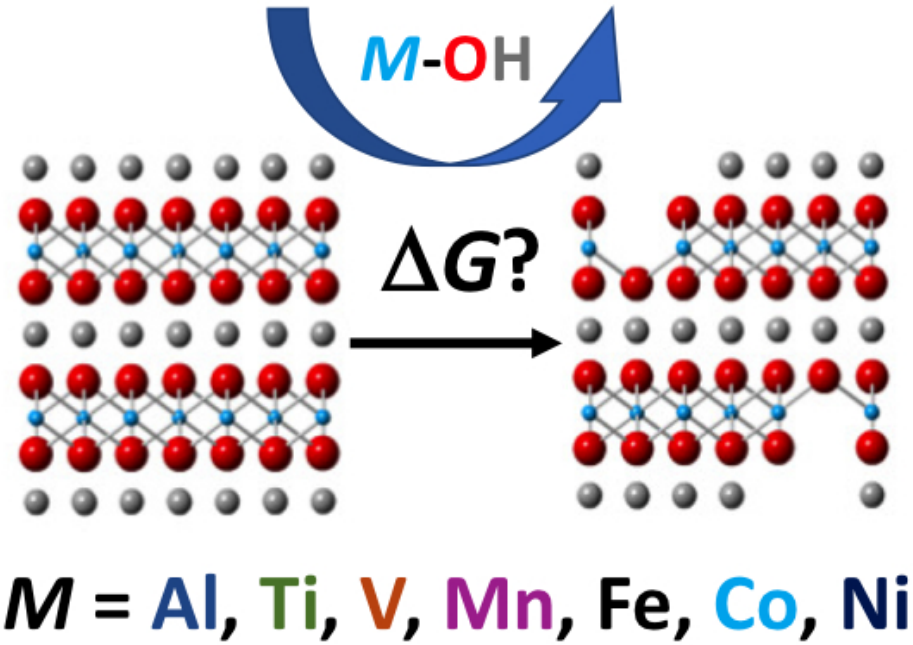

98x68mm (150 x 150 DPI)